Author Manuscript

Author Manuscript

Author Manuscript

Author Manuscript

HHS Public Access

Author manuscript

Cardiovasc Eng Technol. Author manuscript; available in PMC 2018 March 01.

Published in final edited form as:

Cardiovasc Eng Technol. 2017 March ; 8(1): 3–16. doi:10.1007/s13239-016-0291-9.

Finite Element Analysis of Patient-Specific Mitral Valve with Mitral Regurgitation

Thuy Pham[1], **Fanwei Kong**[1], **Caitlin Martin**[1], **Qian Wang**[1], **Charles Primiano**[2], **Raymond McKay**[2], **John Elefteradies**[3], and **Wei Sun**[1]

[1]Tissue Mechanics Laboratory, The Wallace H. Coulter Department of Biomedical Engineering, Georgia Institute of Technology and Emory University, Atlanta, GA

[2]Cardiology Department of Hartford Hospital, Hartford, CT

[3]Aortic Institute of Yale-New Haven Hospital, New Haven, CT

Abstract

Functional mitral regurgitation (FMR) is a significant complication of left ventricular (LV) dysfunction and strongly associated with a poor prognosis. In this study, we developed a patient-specific finite element (FE) model of the mitral apparatus in a FMR patient which included: both leaflets with thickness, annulus, chordae tendineae, and chordae insertions on the leaflets and origins on the papillary muscles. The FE model incorporated human age- and gender- matched anisotropic hyperelastic material properties, and MV closure at systole was simulated. The model was validated by comparing the FE results from valve closure simulation with the *in vivo* geometry of the MV at systole. It was found that the FE model could not replicate the *in vivo* MV geometry without the application of tethering pre-tension force in the chordae at diastole. Upon applying the pre-tension force and performing model optimization by adjusting the chordal length, position, and leaflet length, a good agreement between the FE model and the *in vivo* model was established. Not only were the chordal forces high at both diastole and systole, but the tethering force on the anterior papillary muscle was higher than that of the posterior papillary muscle, which resulted in an asymmetrical gap with a larger orifice area at the anterolateral commissure resulting in MR. The analyses further show that high peak stress and strain were found at the chordal insertions where large chordal tethering forces were found. This study shows that the pre-tension tethering force plays an important role in accurately simulating the MV dynamics in this FMR patient, particularly in quantifying the degree of leaflet coaptation and stress distribution. Due to the complexity of the disease, the patient-specific computational modeling procedure of FMR patients presented should be further evaluated using a large patient cohort. However, this study provides useful insights into the MV biomechanics of a FMR patient, and could serve as a tool to assist in pre-operative planning for MV repair or replacement surgical or interventional procedures.

Correspondent author's contact information: Wei Sun, Ph.D., The Wallace H. Coulter Department of Biomedical Engineering, Georgia Institute of Technology and Emory University, Technology Enterprise Park, Room 206, 387 Technology Circle, Atlanta, GA 30313-2412, Phone: (404) 385-1245, Fax: (404) 894-4243, wei.sun@bme.gatech.edu.

Conflicts of Interest: None.

Ethical Approval: No human studies were carried out by the authors for this article. No animal studies were carried out by the authors for this article.

Author Manuscript Author Manuscript Author Manuscript Author Manuscript

Keywords

Multi-slice Computed Tomography; Mitral valve; Mitral Regurgitation; Chordae Tendineae; Finite Element Simulation; Patient-Specific

1. Introduction

Functional mitral regurgitation (FMR) is a significant complication of left ventricular (LV) dysfunction and strongly associated with a poor prognosis in patients with heart failure. Ischemic mitral regurgitation (IMR) is a form of FMR that results from ventricular abnormality while the mitral leaflets and subvavular apparatus are normal. In IMR, pathological LV remodeling contributes to the apical, posterior, and lateral displacement of papillary muscles, with reduced LV contractility and abnormal annular contraction. The displacement of papillary muscles results in traction on the mitral leaflets and restriction on leaflet motion. Moreover, inadequate closure of the mitral valve (MV) contributes to increased tethering forces and reduced leaflet closing force [1,2]. Severe FMR is associated with high risk of heart failure[3] and mortality[4].

Currently FMR is typically treated through annuloplasty with an undersized ring, but mitral insufficiency can recur in a significant number of cases[5,6]. Other treatments include surgical leaflet resection, chordal shortening or replacement, and edge-to-edge repair[7-11]. The highly complex structure and the interrelated function among the valve substructures, as well as the continuous remodeling mechanism of MR, make MV treatment challenging. Particularly for MV repair, the success of a technique may be associated with increased leaflet stress, mitral annulus force, and chordal forces[12-14]. Therefore, it is important to understand the *in vivo* mechanics and dynamics of the MV for MR patients, in order to assess the effectiveness of surgical repair strategies and determine the optimal strategy available for specific patients.

Computational simulations using numerical analysis methods have been useful in assessing the MV mechanics under normal and diseased conditions as well as evaluating surgical MV repair techniques. A number of studies[15-18] compared different geometries of annuloplasty rings on MR models. Recent advancements in clinical imaging modalities have enabled the development of patient-specific models. MV repair by annuloplasty and MitraClip intervention was studied using patient-specific MV models derived from 3D transesophageal echocardiography (TEE) data[19-21]. However, due to the limited resolution of TEE data, the locations of chordal insertion points and single-point chordal origins on the papillary muscles in these models were assumed. Our recent study has shown that papillary muscle and mitral annulus motions from diastole to systole are essential to accurately simulate leaflet closing behaviors in healthy patient-specific MV models[22]. Realistic chordae and leaflet reconstruction has been achieved based on Micro-CT, but Micro-CT cannot be applied in clinical settings[23]. Hence, in this study, we reconstructed a patient-specific MV computational model from CT image data for a MR patient which includes the motion of the chordal origins and annulus from diastole to systole, as well as accurate leaflet geometry and thickness.

Author Manuscript Author Manuscript Author Manuscript Author Manuscript

Despite the presence of traction on the MV leaflets caused by displacement of the papillary muscles in FMR, the initial geometries, constructed from clinical images, were assumed stress-free in previous studies[15-18]. In this study, we introduced the tethering pre-tension force, the tension existing in the chordae tendineae prior to systole, which plays an important role in accurately simulating the MV dynamics in this FMR patient. Our model incorporated age- and gender- matched anisotropic hyperelastic material models to accurately describe the MV tissue behavior, and the model was validated by comparing the FE results with the *in vivo* CT images at systole. MV measurements and forces generated during diastole and systole were obtained and compared to the literature.

2. Patient and Methods

2. 1 Patient Information

Full-phase cardiac multi-slice Computed Tomography (MSCT) scans of a 71 year old male patient were collected from Hartford Hospital (Hartford, CT). The use of de-identified patient imaging data for this study was approved by the Institutional Review Board at Hartford Hospital (Hartford, CT). The patient was referred for transcatheter aortic valve replacement (TAVR) due to severe aortic stenosis and was also diagnosed with severe MR from Echocardiogram images. Fig. 1A shows the MR jet during systole. The MV leaflets appeared to be mildly thickened. Particularly, the posterior mitral leaflet appeared abnormal —it was tented apically and stationary in systole (Fig. 1B) and diastole (Fig. 1C). From the M-mode (motion mode) ultrasound images the restricted posterior leaflet motion and reduced leaflet copatation was visualized. The LV thickness was normal, but the chamber was dilated with severe regional global hypokinesis, such that the inferior wall was akinetic. The left ventricular ejection fraction (LVEF) was estimated to be 25%, and the LV systolic pressure was 114 mmHg at the time of imaging. The MR radius measured by proximal isovelocity surface area (PISA) was 0.6 cm. The MR Alias velocity was 38.5 cm/s. The left ventricular outflow tract (LVOT) cross-sectional area was 3.8 cm^2 and the stroke volume from the apical 2-chamber view was 33 mL.

2. 2 Model reconstruction

CT images—Full-volume CT image data with ECG gating were acquired with a GE LightSpeed 64-channel volume CT scanner, with a collimation of 25-30 × 0.625 mm. The rotation time of 375 ms resulted in a temporal resolution of less than 200 ms depending on the heart rate and pitch. A total of 2,430 images were collected and reconstructed into 10 phases throughout a cardiac cycle. The images from both middle diastole and middle systole phases were used in the analysis, and will be referred to as simply diastole and systole in the subsequent text. Image segmentation was performed using Avizo (Version 8.0, Burlington, MA) software, where the anterior mitral leaflet (AML), posterior mitral leaflet (PML), mitral annulus (MA), chordae tendineae (chords), papillary muscles (PPMs), chordae insertion points and chordae origins were visualized, identified, and manually segmented[22]. The surface geometries in both diastolic and systolic phases were then imported into HyperMesh (Altair Engineering, Inc., MI) software for 3D mesh generation.

Author Manuscript Author Manuscript Author Manuscript Author Manuscript

Mitral annulus and leaflets—The aorta-mitral fibrous region of the anterior annulus was identified as the junction between the aortic leaflet and the AML, and between the left and right trigones. The posterior annulus was identified at the hinge point of the PML, separating the left atrium from the LV. The anterolateral and posteromedial commissural leaflets were partially visible in CT images; thus, spline surfaces were used to generate the complete geometries of these leaflets. Two layers of solid elements (eight-node hexahedral C3D8I and six-node tetrahedral C3D6 elements) were used to model the leaflets. The morphology of the leaflet was clearly visible, thus, the entire leaflet thickness was traced and measured. For the AML, the average thickness values for the leaflet belly and edge were 1.26 mm and 2.09 mm respectively. For the PML, the average thickness values of the leaflet belly and edge were 1.31 mm and 1.57 mm respectively. The leaflet belly and edge regions were identified as previously described [24].

Chordae Tendineae—A total of 24 chords were visible on CT images. Chords were classified into five groups[22,25]: anterior strut (AS), anterior basal (AB), anterior marginal (AM), posterior basal (PB), and posterior marginal (PM). Chords originated from the anterolateral and posterolateral papillary muscles and inserted into the ventricular surfaces of the leaflets. Contraction of the LV also triggers the contraction of the papillary muscles. Thus, the locations of the chordal insertions and origins change from one phase to another. The chordal insertions and origins were therefore identified in both diastolic and systolic phases and their dynamic motion was accounted for in the simulation. The basal chordal insertion points on the PML were not visible in MSCT images due to the severe tethering, therefore the initial locations were approximated based on published data[25,26]. The total of 18 chordal origins could be detected. The chordal distribution is shown in Table 1.

The chords were modeled using 3D stress/displacement truss elements (two-node linear T3D2 elements), with cross-sectional area values of 0.71 mm^2, 2.05 mm^2, and 0.38 mm^2 assigned to the basal, strut, and marginal chordae, respectively[27]. Branching of the chordae at the insertion points on the leaflets was modeled by creating fork-shaped truss elements, to avoid stress concentration on the leaflets. Each chord was modeled with up to 10 elements with average element length of 1.5 mm.

2. 3 Constitutive Modeling of Mitral Tissues

The material properties of the MV apparatus were obtained from an age- and gender-matched cadaver heart, i.e., 69 year old patient, from our previously published studies of human MV leaflets[24] and chordae tendineae[27] material characterization. Figure 2 shows the stress-strain curves from an equibiaxial protocol of the AML and PML leaflets in both directions and of four chords (AB was assumed to be equivalent to PB). An anisotropic hyperelastic material model was adopted to characterize the mechanical behaviors of the mitral leaflet tissues. The model is based on the fiber-reinforced hyperelastic material model proposed by Holzapfel *et al*[28,29]. Briefly, the mitral tissues were assumed to be composed of a matrix material with two families of embedded fibers, each with a preferred direction. The fiber directions can be mathematically described using two unit vectors. The strain invariant I_1 is used to describe the matrix material; the strain invariant I_{4i} is used to describe the

Author Manuscript Author Manuscript Author Manuscript Author Manuscript

properties of the fiber families and equals to the squares of the stretches in the fiber directions. The strain energy function W can be expressed as

$$W=C_{10}\{\exp[C_{01}(\overline{I_1}-3)]-1\}+\frac{k_1}{2k_2}\sum_{i=1}^{2}[\exp\{k_2[\kappa\overline{I_1}+(1-3\kappa)\overline{I_{4i}}-1]^2\}-1]+\frac{1}{D}(J-1)^2, i=1,2 \quad (1)$$

where, C_{10}, C_{01}, k_1, k_2 and D are material constants. C_{10} and C_{01} are used to describe the matrix material. D is the material constant that introduces the near incompressibility, while k_1 is a positive material constant with the dimensions of stress and k_2 is a dimensionless parameter. In addition, a dispersion parameter κ was used to describe the distribution of fiber orientation. When κ=0, the fibers are perfectly aligned (no dispersion). When κ=1/3, the fibers are randomly distributed and the material becomes isotropic. The anisotropic hyperelastic material model was implemented into Abaqus 6.13(SIMULIA, Providence, RI) with a user sub-routine VUMAT [30]. Details on the model implementation were previously published by our group [22,30,31]. Local coordinate systems were defined for each leaflet to include fiber orientations for each region.

The isotropic hyperelastic Ogden material model was used to characterize the mechanical properties of chords based on the experimental data[27]. The material constants were determined using SYSTAT (Systat Software Inc., Chicago, IL) with the Marquardt-Levenberg algorithm to fit the uniaxial test results of chordae tendineae to the Ogden model. Table 2 lists the patient information and the fitted material parameters for the mitral tissues.

A material sensitivity analysis was performed to investigate the effect of different material properties on MV response. The material properties of the MV leaflets and chordae were obtained from our previous publication [24,27]. These material properties were either more compliant or stiffer than the one with age- and gender-matched, to observe whether the extremities would affect the results.

2. 4 Boundary and loading conditions

The motion and dynamics of the MV during closing was simulated in two steps. In the first step, the dynamic motions of the mitral annulus from diastole to systole were simulated by imposing kinematic displacement of the nodes along the mitral annulus. The chordal origin nodes were also displaced between the two phases. In the second step, time-varying physiological transvalvular pressure loading, with a maximum systolic pressure of 114 mmHg, was applied on the ventricular surfaces of the AML and PML. All simulations were performed in ABAQUS Explicit (Version 6.13).

2. 5 Model Optimization and Validation

To validate the FE model accuracy, the distance error between the deformed FE model and the “true image” model obtained from systolic MSCT images was computed in MATLAB.

Author Manuscript Author Manuscript Author Manuscript Author Manuscript

The distance errors were obtained by first projecting the deformed (systolic) FE model on to the true image model, then the distance error could be computed as the point-to-mesh distance between the nodes of the deformed FE mesh and their corresponding projected nodes on the true image model. A point-to-mesh distance greater than 2 mm was considered unacceptable and required further model adjustment. The method of calculating the distance error based on the point-to-mesh difference between the FE deformed and true image model has been recently published by our group in a previous publication [32].

Due to the limitation of the CT image resolution, it was not possible to detect all of the chords or the accurate chordal length. Therefore, the number of chords and their lengths were estimated in the initial model and required optimization. The model was adjusted until the deformed FE model could closely match the true image model. Figure 4 illustrates the FE model optimization workflow, showing the FE simulation steps and criteria for model adjustment. If the surface of the valve leaflets were protruding towards the left atrium in FE deformed model at systole, with distance errors larger than 2 mm, the chords in the vicinity were shortened. If a chord was excessively tensioned and stretched the leaflet, it was then elongated. The chordal lengths were adjusted while keeping the insertion and origin points unchanged.

After 20+ iterations, the length of the chords had been minimized, as shown in Fig. 5A, yet several regions on the deformed FE model still did not match the true image model, particularly the belly region of the AML, the entire PML, and the two commissural leaflets, see Fig. 5C & 5D. The point-to-mesh distance map in Fig. 5B shows the regions with straightened chords that exhibited errors greater than 2 mm. These large errors indicated that adjusting the chordal length alone was insufficient to accurately simulate the systolic MV deformation. Therefore, an existing chordal tethering force at diastole due to dilatation of the LV in this FMR patient, which could further restrict the leaflet motion, was assumed. This pre-existing force was generated by shortening the length of the tethered chords by 1.99 mm on average in a total of 8 chords. The chordal origins were translated towards the annulus plane along the vector going from the chordal origin point to the insertion point by the magnitude of the chordal shortening. Hence, an additional step of pretension was added to the simulation process, where the translated origins were displaced from their adjusted locations to their original locations identified from MSCT to generate the pre-tension in the chords, see Fig. 4. Approximately 50 iterations were performed to optimize the chordal lengths and degree of pre-tension.

The application of pre-tension pulled and elongated the PML towards the papillary muscles. Therefore, the PML in deformed FE model was longer than in the true image model. In order to compensate for the post-pretension leaflet elongation, the degree of radial elongation throughout the PML was measured, and the un-deformed PML geometry was then shrunk radially by the same elongation ratio. After this adjustment, the FE deformed PML geometry could match that obtained from *in vivo* MSCT images at diastole. The PML thickness at the P2 section before and after the leaflet shrinking was 1.32 and 1.17, respectively, which is within the CT image resolution of 0.625 mm. Therefore, we ignored the leaflet thickness change.

Author Manuscript Author Manuscript Author Manuscript Author Manuscript

2.6 Data analysis

MV measurements in diastole and systole were made from the FE and true image. The anteroposterior (AP) distance was measured as the distance between the midpoint of the intertrigonal region and the midpoint of the posterior annulus[22]. The intercommissural (IC) distance was measured as the distance between the two commissure leaflets. The distances between the PM tips were measured in both the apical-base and lateral-medial directions. The total mitral annular perimeter and area and the lengths of the anterior and posterior annuli were measured. The coaptation depth and length were calculated as the perpendicular distance from the annular plane down to the coaptation point, and from the coaptation point to the leaflet edges, respectively[33]. The annular height was measured as the maximal vertical distance between the highest (anterior or posterior) and lowest (anterolateral or posteromedial) points[32]. The systolic MV orifice areas for both the FE deformed and true image model were measured and compared. The tenting area and volume during mid systole were also measured during systole[34,35]. The reaction force at the chordal origins, as well as the stress and strain on the leaflets were output from the FE simulation.

3. Results

3.1. Patient valve geometry measurements

Table 3 displays the MV measurements obtained from the MSCT images at diastole and systole. The measurements were compared to those in literature for normal and FMR patients. At diastole, the anterior and posterior mitral leaflets areas in the FE model were 804.2 mm^2 and 779.6 mm^2 respectively. The maximum radial lengths of the AML and PML were 30.0 mm and 15.4 mm, respectively. The typical saddle-shaped annulus was not present in this model. In contrast, the annulus appeared almost flat, with little change in the annular height from diastole to systole. Figure 3 displays the division of the mitral valve leaflets into three regions, where 1 is the anterolateral, 2 is the middle, and 3 is the posteromedial section. The table in Fig. 3 includes the tenting angle of the leaflets during systole. Large PML tenting angles of 53 and 73 degrees at P1 and P2 respectively, prevented coaptation with the AML at the leaflet free-edge. Distortion of the papillary muscle geometries was evident (Table 3): the distance between the APM and the left trigone of 31.65 mm was greater than the distance between the PPM and the right trigone of 27.74 mm. These values, especially the APM to left trigone distance, deviated from the normal ranges measured experimentally, where the APM to left trigone distance is 23.5 ± 3.7 mm and the PPM to right trigone distance is 23.5 ± 4.0 mm[36]. The distance between the APM and PPM was 38.73 laterally and 0.14 apically at diastole, and 36.61 mm laterally and 0.42 mm apically in systole.

3.2. FE Simulation Results

Figure 6 shows the final optimized geometries of the MV after performing chordal optimization, applying chordal pre-tension, applying annulus and papillary boundary conditions, and applying systolic pressure. The atrial, sagittal and isometric views of the valve in Figs. 6A to C demonstrated a good agreement between the FE deformed MV and the true image model at systole. During peak systole, a large regurgitant orifice was visible at the P1 and partial P2 regions. Figure 6D displays an overlay of the 2D projections of the

Author Manuscript Author Manuscript Author Manuscript Author Manuscript

regurgitant orifice in the FE deformed and true image models at systole. The 2D areas from the FE model and true image model were 60.55 and 51.86 mm^2, respectively. At diastole, the total chordal tethering forces were 16.30 and 2.70 N for APM and PPM, respectively. At the peak systolic pressure, the total forces on the APM and PPM were 9.41 N and 4.50 N, respectively. The average systolic chordal tension forces were compared to *in vitro* force data obtained from Jimenez et al.[37]in Table 4.

The mean point-to-mesh distance between the FE deformed model and the true image model was 0.96 ± 0.82 mm, indicating a good agreement between the two models. The model can capture most of the AML leaflet deformation, from the fibrosa toward the belly region. Larger errors between 2 and 4 mm were found along the free edge of the commissure leaflets. Most regions of the PML were well captured including the tethered regions of P1 and partial P2, with less than 1 mm errors. The largest error was located at the free edge region of the posteromedial commissure leaflet (P3).

Figure 7 shows the stress and strain distributions of the MV components at peak systolic pressure. After removing the 1% peak stress[38], the maximum principal stress (MPS) of the AML was 1.62 MPa at the left and right trigone regions on the ventricular surface of AML. On the AML leaflet, high stresses were also distributed along the fibrosa region towards the strut chord insertions. The MPS of the PML was 1.51 MPa, and similar to the AML, was located at the P2 annular region.

The maximum principal strain (MPe) for the AML was 0.40 at the trigones, and a high strain value of 0.28 was observed at the tethered chord insertion regions. The MPe for the PML was 0.36 at the tethered chord insertion regions, near the free-edge and basal locations. Overall, at the regions with significant tethering, stress and strain on PML (P1 and P2 regions) exceeded that of AML, for instance, peak values were ranging from 0.15 to 0.32 strain and 0.22 to 1.51 MPa stress compared to 0.03 to 0.15 strain and -0.11 to 0.53 MPa on AML. High stress and large stretch on PML correspond to the phenomenon of posterior leaflet motion restriction observed clinically.

The stress-strain curves in Fig. 8a & b show that for AML the Material 3 (blue) was much softer than the original Material 1 (red) in both circumferential and radial directions, and the Material 2 (green) was stiffer than the original Material 1 in the radial direction but comparable in the circumferential direction. Similarly, the PML tissue properties of Material 3 were softer in both directions, and the Material 2 was stiffer in the radial direction. The simulation results in Fig. 8c show that without applying pretension tethering forces, there was more coaptation at the regurgitant zone—the leaflets were almost closed in the original and Material 3 models. With pretension, as shown in Fig. 8d, the Material 2 exhibited a larger gap, whereas smaller gap was observed in the softer Material 3 model. Furthermore, as shown in Fig. 8e & f, the effects of varying material properties were negligible for PML where there was no change in distance error among the three models. For AML, however, the softer Material 3 exhibited a largest mean distance error compared to others. The difference in distance error between with pretension (yellow) and without pretension (red) was more pronounced in PML compared to AML. The systolic chordal forces of the models with stiffer and softer materials were comparable to that of the original model. The chordal

Author Manuscript Author Manuscript Author Manuscript Author Manuscript

systolic forces on APM were 9.41 N, 11.72 N, and 8.07 N for the original, stiffer and softer materials, respectively. The chordal systolic forces on PPM were 4.50 N, 3.94 N and 4.77 N on PPM, for the original, stiffer and softer materials, respectively. However, the diastolic chordal forces showed an exceedingly large variation depending on material properties. Therefore, applying pretension on chords and leaflets were effective to mimic valve closure for a range of human material properties, whereas highly matched material properties are required to obtain reliable pretension chordal forces at diastole.

4. Discussion

In this study, we developed a patient-specific MV model of a patient with severe MR. Echo images showed the patient exhibited a large MR yet, restricted posterior leaflet motion and dilated LV. Both restricted PML and LV enlargement resulted in large PML angles at P1 and P2 locations. According to a study by Magne *et al.*[39], a patient with this large PML angles might have significant risk factors of recurrent MR and poor long-term outcomes after MV repair. The FE model developed in this study was able to accurately captured PML tethering by accounting for the pre-tension tethering forces in the chordae tendineae and the mitral leaflets. We observed high chordal forces on the tethering papillary muscles at both diastole and systole, as well as increased stress and strain on the tethering PML.

Early experiments have suggested that tension on chordae tendineae and mitral leaflets existed not only at systole but also diastole[40,41]. For MR patient, LV dilation and apical displacement of papillary muscles could cause more traction on leaflets and thus prevent proper coaptation. Systolic chordal forces as well as leaflet stress and strain values have been studied both experimentally and computationally by simulating an MR state of mitral valve[17,30,37,42]. However, few studies have looked into the tension that exists in diastole in IMR patient due to papillary muscle traction, and MV models at diastole state have mostly been assumed stress free[17,19,30,43]. For this patient, a lack of annulus and ventricular contraction, large tenting angle and area were observed from MSCT images, as well as restricted PML motion from diastole to systole. From our simulation, we found that ignoring the tension in chords and leaflets during diastole would overestimate the leaflet coaptation for this MR patient, and 84% larger in average point-to-mesh distance error compared to the model with pretension. The results indicated that the existing pre-tension force in chords and leaflets at diastole was essential in accurately replicating the in vivo MV geometries at systole.

Altered balance between chordal tethering force and leaflet coaptation force upon transvalvular pressure during systole contributes to improper leaflet coaptation[44]. We found a higher chordal tethering force on APM (16.30 N at diastole and 9.41 N at systole) than on PPM (2.70 N at diastole and 4.50 N at systole). The imbalanced force distribution between two PPMs contributed to the larger regurgitant gap on the anterolateral side in systole. Moreover, the tethering force, required in diastole in order to match with the true systole geometry obtained from *in vivo* MSCT scans, caused a posteriorly shifted coaptation line as well as large tenting angle on PML. We also observed a decreased in the total chordal force on APM from diastole to systole. That could be due to the reduced relative distance between the APM tip and annulus in systole, which was observed from the MSCT images for this

Author Manuscript Author Manuscript Author Manuscript Author Manuscript

patient. Despite of the lack of saddle shape, the annulus for this patient moved towards the apex in systole due to active contraction[37,40,41]. The reduction of relative distance released the tension on chords and leaflets, counteracting the coaptation force due to pressure in systole.

A material sensitivity analysis was performed using a stiffer set and a softer set of material properties. For each material set, the point-to-mesh distance errors from simulations with pretension and without pretension were compared. Increased distance errors were observed on models without pretention for all materials, together with incorrectly increased coaptation and leaflet protrusion toward the left atrium, see Figure 8. The systolic chordal forces were comparable with the original model (11.72 N and 8.07 N on APM; 3.94 N and 4.77 N on PPM, for stiffer and softer materials, respectively). However, the diastolic chordal force showed large variation depending on material properties. Therefore, applying pretension on chords and leaflets were effective to mimic valve closure for a range of human material properties, whereas highly matched material properties are required to obtain reliable pretension chordal forces at diastole.

Although the leaflet and chordae tendineae materials were age- and gender- matched, they were not determined from the same MR patient. Therefore, we investigated the effects of different sets of material parameters on the patient MV function and on the pretension forces. We showed that different material properties showed different MV response. However, variation in material parameters were negligible in the affected tethering region, in which the PML of this model. Furthermore, distance errors were higher on models without pretention, incorrectly increased coaptation and leaflet protrusion towards the left atrium. A large difference in distance error between with pretension and without pretension on PML compared to AML also indicated more error could be obtained at the tethering region of the valve leaflets when pretension is not considered. Nevertheless, material properties determined inversely from CT images would be ideal to obtain accurate biomechanics data.

We have demonstrated that pre-tension force existed within this MR patient who had LV dilation and leaflet tethering. However, we only analyzed one patient in this study. Functional MR is a complicated disease with a large spectrum of etiologies ranges from upper region of annular dilatation, leaflet alternation due to tethering, to lower left ventricular distortion. Thus, patient-specific computational modeling of MR patient, particularly functional MR group, need to be further studied and the modeling procedures should be further evaluated using a large patient cohort. Although chords were traced from MSCT images, due to limited resolution of the current cardiac images, image digitalization, segmentation and model optimization methods were utilized to adjust chordal length. The number of chords, chordal insertion and origins, and branching patterns were determined based on CT images which were insufficiently clear to capture detailed structure and prone to human digitization errors. Active stiffening of AML was not accounted for in our model, while modeling active muscle contraction may prevent billowing of AML and provide better match between the deformed geometry and the ground truth[45].

Author Manuscript Author Manuscript Author Manuscript Author Manuscript

5. Conclusion

This study shows that the incorporation of pre-tension tethering forces improved modeling accuracy and allowed evaluation of MV dynamic function. A computational method was carried out to optimize the chordal length in combination of adjusting the leaflet height to model the effect of pre-tension. The results obtained show that the simulated model can closely replicate the *in vivo* geometry of the MV at systole from MSCT images. We found that not only the chordal forces were high at both diastole and systole, the total chordal tethering force on the anterior papillary muscle was higher than that of the posterior papillary muscle, which resulted in an asymmetrical gap with larger orifice area at the anterolateral commissure that caused MR. The analyses show that high peak stress and strain were observed at the chordal insertions where large chordal forces were found. This study provides a quantitative evaluation of MV function in a FMR patient that could be useful in pre-procedural planning for an effective MV repair or replacement surgical or interventional treatment.

Acknowledgments

Research for this project was funded in part by NIH HL104080 and HL127570. Fanwei Kong was also supported in part by the Petit Scholar program at Georgia Institute of Technology.

References

1. Iung B. Management of ischaemic mitral regurgitation. Heart. 2003; 89:459–464. [PubMed: 12639884]
2. Piérard LA, Carabello BA. Ischaemic mitral regurgitation: pathophysiology, outcomes and the conundrum of treatment. 2010
3. Trichon BH, Felker GM, Shaw LK, Cabell CH, O'Connor CM. Relation of frequency and severity of mitral regurgitation to survival among patients with left ventricular systolic dysfunction and heart failure. American Journal of Cardiology. 2003; 91:538–543. [PubMed: 12615256]
4. Taramasso M, Maisano F. Valvular disease: Functional mitral regurgitation: should all valves be replaced? Nat Rev Cardiol. 2016; 13:65–66. [PubMed: 26727300]
5. Tahta SA, Oury JH, Maxwell JM, Hiro SP, Duran CM. Outcome after mitral valve repair for functional ischemic mitral regurgitation. J Heart Valve Dis. 2002; 11:11–18. discussion 18-19. [PubMed: 11858163]
6. McGee EC Jr, Gillinov AM, Blackstone EH, et al. Recurrent mitral regurgitation after annuloplasty for functional ischemic mitral regurgitation. The Journal of thoracic and cardiovascular surgery. 2004; 128:916–924. [PubMed: 15573077]
7. Glower DD. Surgical Approaches to Mitral Regurgitation. Journal of the American College of Cardiology. 2012; 60:1315–1322. [PubMed: 22939558]
8. Acker MA, Parides MK, Perrault LP, et al. Mitral-Valve Repair versus Replacement for Severe Ischemic Mitral Regurgitation. New England Journal of Medicine. 2014; 370:23–32. [PubMed: 24245543]
9. Goldstein D, Moskowitz AJ, Gelijns AC, et al. Two-Year Outcomes of Surgical Treatment of Severe Ischemic Mitral Regurgitation. New England Journal of Medicine. 2016; 374:344–353. [PubMed: 26550689]
10. Nicolini F, Agostinelli A, Vezzani A, et al. Surgical treatment for functional ischemic mitral regurgitation: current options and future trends. Acta Biomed. 2015; 86:17–26. [PubMed: 25948023]
11. de Oliveira J, Antunes MJ. Mitral valve repair: better than replacement. Heart. 2006; 92:275–281. [PubMed: 16415204]

Author Manuscript Author Manuscript Author Manuscript Author Manuscript

12. Bothe W, Kvitting JP, Swanson JC, et al. How do annuloplasty rings affect mitral leaflet dynamic motion? Eur J Cardiothorac Surg. 2010; 38:340–349. [PubMed: 20335042]
13. Jensen MO, Jensen H, Smerup M, et al. Saddle-shaped mitral valve annuloplasty rings experience lower forces compared with flat rings. Circulation. 2008; 118:S250–255. [PubMed: 18824763]
14. Laing G, Dupont PE. Beating-heart Mitral Valve Chordal Replacement. Conference Proceedings. 2011; 2011:2476–2479. [PubMed: 22254843]
15. Maisano F, Redaelli A, Soncini M, et al. An Annular Prosthesis for the Treatment of Functional Mitral Regurgitation: Finite Element Model Analysis of a Dog Bone–Shaped Ring Prosthesis. The Annals of Thoracic Surgery. 2005; 79:1268–1275. [PubMed: 15797061]
16. Kunzelman KS, Reimink MS, Cochran RP. Flexible versus rigid ring annuloplasty for mitral valve annular dilatation: a finite element model. J Heart Valve Dis. 1998; 7:108–116. [PubMed: 9502148]
17. Votta E, Maisano F, Bolling SF, et al. The Geoform Disease-Specific Annuloplasty System: A Finite Element Study. The Annals of Thoracic Surgery. 2007; 84:92–101. [PubMed: 17588392]
18. Wong VM, Wenk JF, Zhang Z, et al. The effect of mitral annuloplasty shape in ischemic mitral regurgitation: a finite element simulation. Ann Thorac Surg. 2012; 93:776–782. [PubMed: 22245588]
19. Choi A, Rim Y, Mun JS, Kim H. A novel finite element-based patient-specific mitral valve repair: virtual ring annuloplasty. Biomed Mater Eng. 2014; 24:341–347. [PubMed: 24211915]
20. Stevanella M, Maffessanti F, Conti C, et al. Mitral Valve Patient-Specific Finite Element Modeling from Cardiac MRI: Application to an Annuloplasty Procedure. Cardiovascular Engineering and Technology. 2011; 2:66–76.
21. Mansi T, Voigt I, Georgescu B, et al. An integrated framework for finite-element modeling of mitral valve biomechanics from medical images: application to MitralClip intervention planning. Med Image Anal. 2012; 16:1330–1346. [PubMed: 22766456]
22. Wang Q, Sun W. Finite element modeling of mitral valve dynamic deformation using patient-specific multi-slices computed tomography scans. Ann Biomed Eng. 2013; 41:142–153. [PubMed: 22805982]
23. Lee, CH., Oomen, PJA., Rabbah, JP., et al. Functional Imaging and Modeling of the Heart: 7th International Conference, FIMH 2013, London, UK, June 20-22, 2013 Proceedings. Sébastien, OurselinDaniel, Rueckert, Nicolas, Smith, editors. Springer Berlin; Heidelberg: 2013. p. 416-424.
24. Pham T, Sun W. Material Properties of Aged Human Mitral Valve Leaflets. J Biomed Mater Res A. 2014; 102:2692–2703. [PubMed: 24039052]
25. Lam JH, Ranganathan N, Wigle ED, Silver MD. Morphology of the human mitral valve. I. Chordae tendineae: a new classification. Circulation. 1970; 41:449–458. [PubMed: 5415982]
26. Wang Q, Sun W. Finite Element Modeling of Mitral Valve Dynamic Deformation Using Patient-Specific Multi-Slices Computed Tomography Scans. Ann Biomed Eng. 2013; 41:142–153. [PubMed: 22805982]
27. Zuo K, Pham T, Li K, et al. Characterization of biomechanical properties of aged human and ovine mitral valve chordae tendineae. J Mech Behav Biomed Mater. 2016; 62:607–618. [PubMed: 27315372]
28. Holzapfel GA, Gasser TC, Ogden RW. A New Constitutive Framework for Arterial Wall Mechanics and a Comparative Study of Material Models. Journal of elasticity and the physical science of solids. 2000; 61:1–48.
29. Gasser TC, Ogden RW, Holzapfel GA. Hyperelastic modelling of arterial layers with distributed collagen fibre orientations. Journal of The Royal Society Interface. 2006; 3:15–35.
30. Wang Q, Primiano C, Sun W. Can isolated annular dilatation cause significant ischemic mitral regurgitation? Another look at the causative mechanisms. Journal of Biomechanics. 2014; 47:1792–1799. [PubMed: 24767703]
31. Sun W, Sacks MS. Finite element implementation of a generalized Fung-elastic constitutive model for planar soft tissues. Biomech Model Mechanobiol. 2005; 4:190–199. [PubMed: 16075264]
32. Liang L, Kong F, Martin C, et al. Machine learning–based 3-D geometry reconstruction and modeling of aortic valve deformation using 3-D computed tomography images. International Journal for Numerical Methods in Biomedical Engineering. 2016:n/a–n/a.

Author Manuscript Author Manuscript Author Manuscript Author Manuscript

33. Gogoladze G, Dellis SL, Donnino R, et al. Analysis of the mitral coaptation zone in normal and functional regurgitant valves. Ann Thorac Surg. 2010; 89:1158–1161. [PubMed: 20338324]
34. Ciarka A, Braun J, Delgado V, et al. Predictors of Mitral Regurgitation Recurrence in Patients With Heart Failure Undergoing Mitral Valve Annuloplasty. The American journal of cardiology. 2010; 106:395–401. [PubMed: 20643253]
35. Dudzinski DM, Hung J. Echocardiographic assessment of ischemic mitral regurgitation. Cardiovascular Ultrasound. 2014; 12:46. [PubMed: 25416497]
36. Sakai T, Okita Y, Ueda Y, et al. Distance between mitral anulus and papillary muscles: anatomic study in normal human hearts. J Thorac Cardiovasc Surg. 1999; 118:636–641. [PubMed: 10504627]
37. Jimenez JH, Soerensen DD, He Z, Ritchie J, Yoganathan AP. Mitral valve function and chordal force distribution using a flexible annulus model: an in vitro study. Ann Biomed Eng. 2005; 33:557–566. [PubMed: 15981857]
38. Pham, TM., DeHerrera, M., Sun, W. Mechanics of Biological Systems and Materials, Volume 2: Proceedings of the 2011 Annual Conference on Experimental and Applied Mechanics. Tom, Proulx, editor. Springer; New York: 2011. p. 1-10.
39. Magne J, Pibarot P, Dagenais F, et al. Preoperative posterior leaflet angle accurately predicts outcome after restrictive mitral valve annuloplasty for ischemic mitral regurgitation. Circulation. 2007; 115:782–791. [PubMed: 17283262]
40. Rushmer RF, Finlayson BL, Nash AA. Movements of the mitral valve. Circ Res. 1956; 4:337–342. [PubMed: 13317029]
41. Yellin EL, Peskin C, Yoran C, et al. Mechanisms of mitral valve motion during diastole. American Journal of Physiology - Heart and Circulatory Physiology. 1981; 241:H389.
42. Jimenez JH, Soerensen DD, He Z, He S, Yoganathan AP. Effects of a saddle shaped annulus on mitral valve function and chordal force distribution: an in vitro study. Ann Biomed Eng. 2003; 31:1171–1181. [PubMed: 14649491]
43. Mansi T, Voigt I, Assoumou Mengue E, et al. Towards patient-specific finite-element simulation of MitralClip procedure. Med Image Comput Comput Assist Interv. 2011; 14:452–459. [PubMed: 22003649]
44. Nielsen SL, Nygaard H, Fontaine AA, et al. Chordal force distribution determines systolic mitral leaflet configuration and severity of functional mitral regurgitation. Journal of the American College of Cardiology. 1999; 33:843–853. [PubMed: 10080490]
45. Skallerud B, Prot V, Nordrum IS. Modeling active muscle contraction in mitral valve leaflets during systole: a first approach. Biomechanics and Modeling in Mechanobiology. 2011; 10:11–26. [PubMed: 20419330]
46. Kunzelman KS, Cochran RP, Verrier ED, Eberhart RC. Anatomic basis for mitral valve modelling. J Heart Valve Dis. 1994; 3:491–496. [PubMed: 8000582]
47. Jimenez JH, Soerensen DD, He Z, Ritchie J, Yoganathan AP. Mitral Valve Function and Chordal Force Distribution Using a Flexible Annulus Model: An In Vitro Study. Annals of Biomedical Engineering. 2005; 33:557–566. [PubMed: 15981857]

Author Manuscript Author Manuscript Author Manuscript Author Manuscript

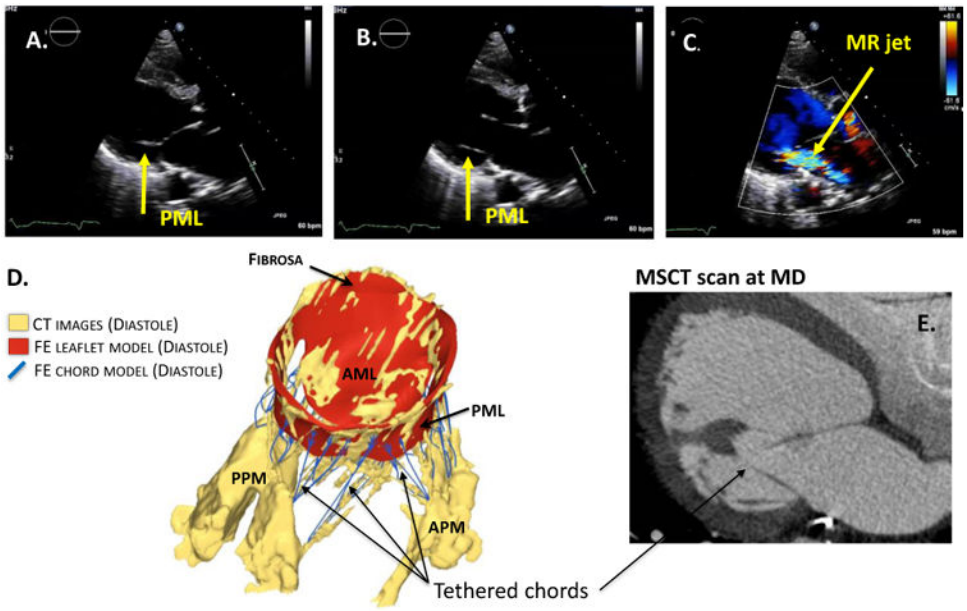

Figure 1.

Patient Echo images of the mitral valve at a) systole and b) diastole, showing the posterior leaflet (PML) is tenting, c) the Doppler Color Echo image displays a large MR jet during systole, d) 3D reconstructed Finite Element (FE) model of leaflets (red) and chordae tendineae (blue) from true CT images (yellow), and e) CT image of the valve during diastole, showing a tethered chord which can be captured in the FE model. AML – Anterior Mitral Leaflet; PML – Posterior Mitral Leaflet; PPM – Posterior Papillary Muscle; APM – Anterior Papillary Muscle; MD – Middle Diastole; MSCT – Multislice CT scan; MR – Mitral Regurgitation.

Author Manuscript
Author Manuscript
Author Manuscript
Author Manuscript

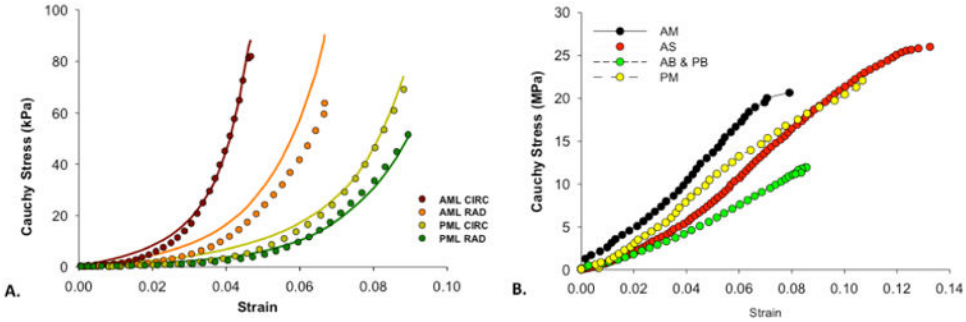

Figure 2.

a) Stress-strain curves of anterior mitral (AML) and posterior mitral leaflet (PML) leaflets under equibiaxial stretch in both circumferential (CIRC) and radial (RAD) directions. The lines show the model fitting results comparing against experimental data; and b) Uniaxial stress-strain curves of anterior marginal (AM), anterior strut (AS), anterior basal (AB), posterior basal (PB) and posterior marginal (PM) chords, and the last data points (arrows) represent the ultimate failure strength.

Author Manuscript Author Manuscript Author Manuscript Author Manuscript

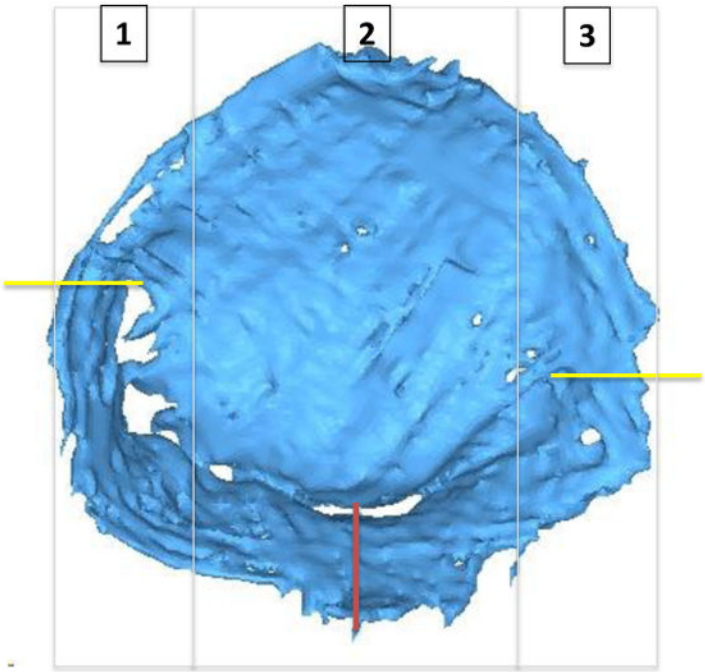

	A1/P1	A2/P2	A3/P3
AML angle (degree)	23	18	15
PML angle (degree)	53	73	40
Tenting area (mm^2)	39.57	111.58	69.29
Tenting volume (mm^3)	3,396		

Figure 3.

Leaflet tenting angles, areas and volumes at three regions, (1) anterolateral, (2) middle, and (3) posteromedial, during systole. Yellow lines indicates commissure clefts and red line is the middle point of the posterior annulus.

Author Manuscript Author Manuscript Author Manuscript Author Manuscript

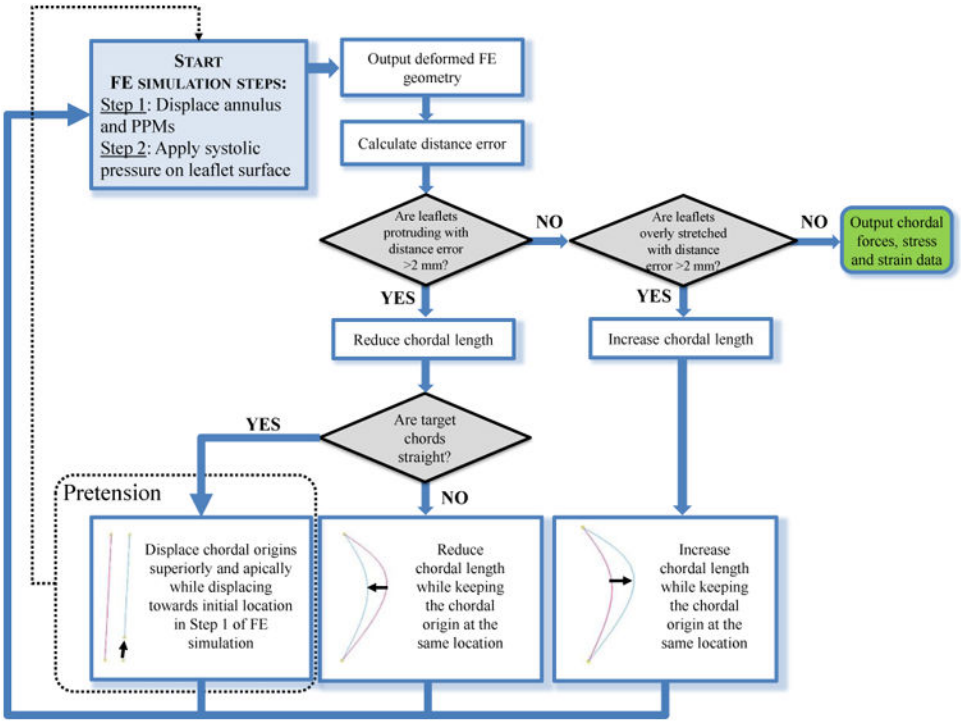

Figure 4.
Flow chart of the Finite Element model optimization.

Author Manuscript Author Manuscript Author Manuscript Author Manuscript

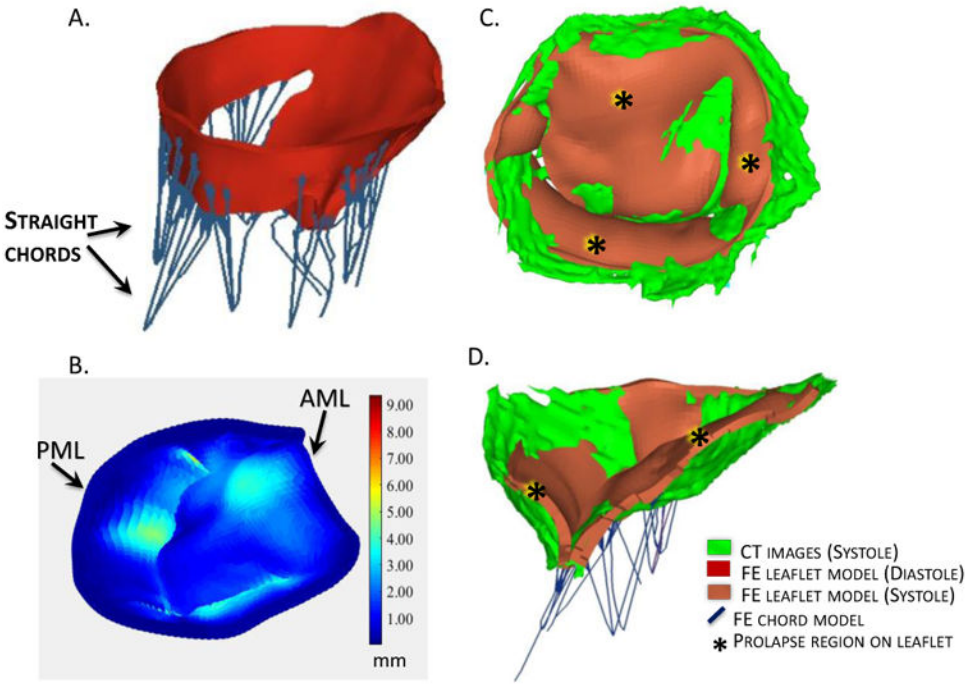

Figure 5.

a) FE model after chordal length optimization at diastole; b) The distance error map between the deformed FE model and the true image model at middle systole; c) top and d) cross-sectional views of deformed FE model overlapping with true image model from CT images at systole after applied the left ventricle pressure and mitral annulus and papillary muscle dynamic motions; the regions of unmatched geometries are labeled with asterisk, in the belly of anterior mitral leaflet (AML) and posterior mitral leaflet (PML).

Author Manuscript Author Manuscript Author Manuscript Author Manuscript

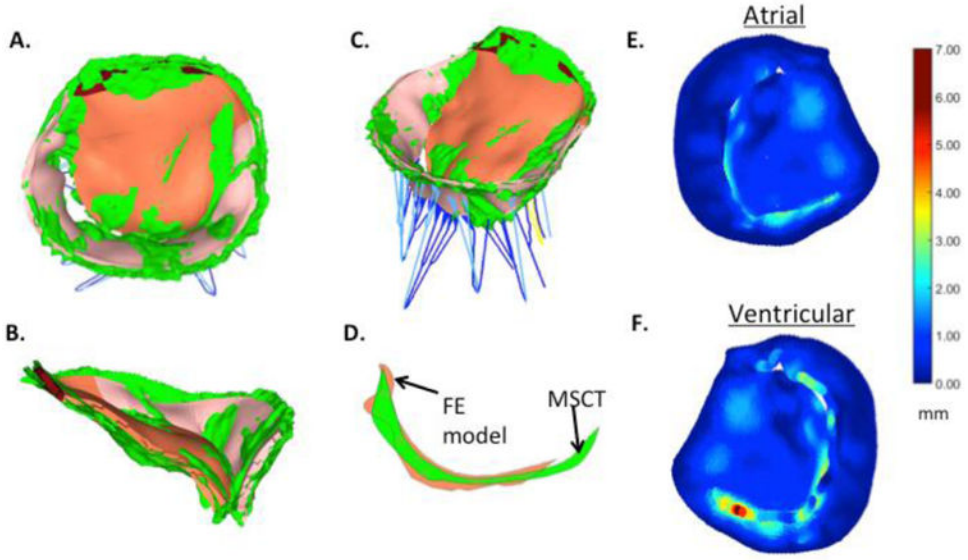

Figure 6.

a) Atrial, b) sagittal and c) isometric views of the deformed FE model (orange for anterior mitral leaflet, light pink for posterior mitral leaflet, and dark red for anterior fibrosa) overlapped with the true image model from MSCT images (green) at middle systole, d) the projected orifice areas of the deformed FE model (orange) and middle-systolic geometry from MSCT images (green); e) atrial and f) ventricular surface views of the calculated distance error maps at middle systole.

Author Manuscript Author Manuscript Author Manuscript Author Manuscript

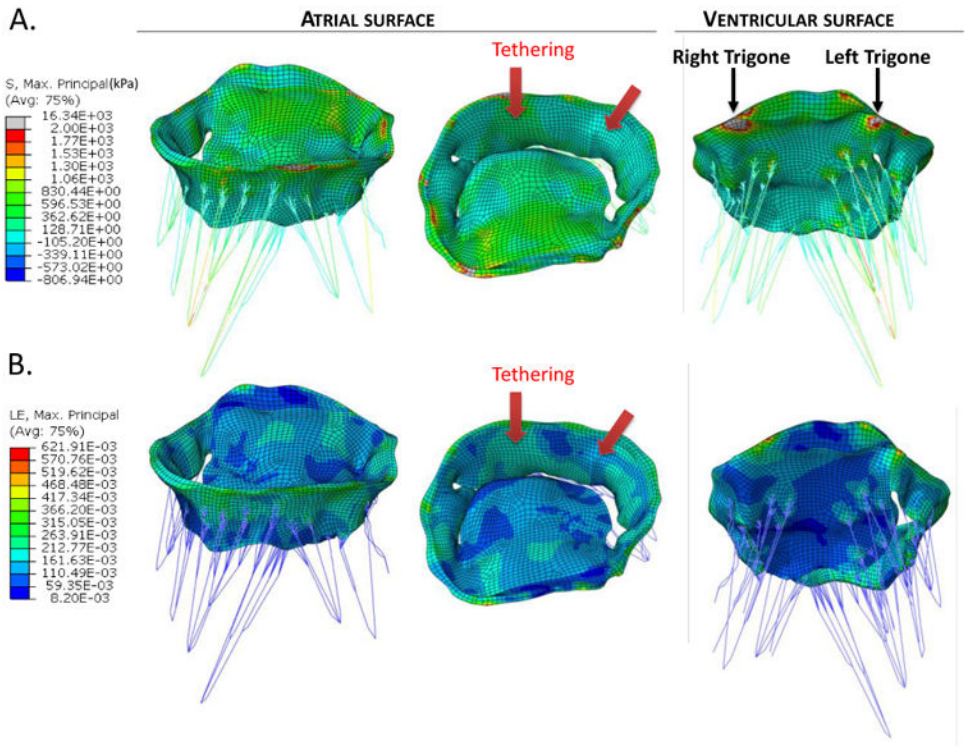

Figure 7.

a) Stress and b) strain distributions of the optimized model of the mitral valve leaflets showing the atrial and ventricular surfaces and tethering locations on the posterior mitral leaflet. Black arrows show the stress at trigone regions. Red arrows show the stress at tethering regions.

Author Manuscript Author Manuscript Author Manuscript Author Manuscript

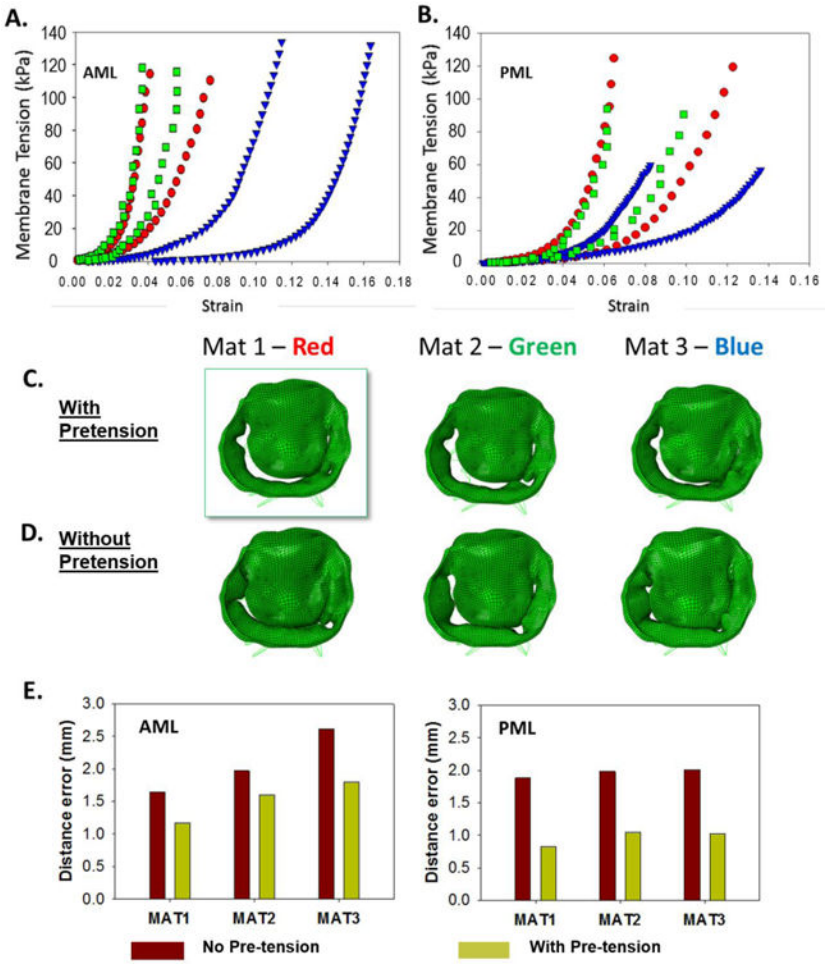

Figure 8.

Stress-strain data of a) AML and b) PML leaflets from three patients under equibiaxial stretch in both circumferential (CIRC) and radial (RAD) directions; the deformed FE model c) with pretension and d) without pretension using the three different material parameter sets; d) the comparison of point-to-mesh distance error between the models with different material properties; e) the average distance errors of the deformed FE models with or without applying pre-tension

Author Manuscript

Author Manuscript

Author Manuscript

Author Manuscript

Table 1

Number of chordal origins on each papillary muscle.

	Current FE Model	Kunzelmen *et al.* [46]
From anterolateral papillary muscle		
To anterior mitral leaflet	4	5.8 ± 1.4
To posterior mitral leaflet	5	6.4 ± 1.7
From posterolateral papillary muscle		
To anterior mitral leaflet	2	4.8 ± 1.5
To posterior mitral leaflet	6	6.2 ± 1.4

Author Manuscript Author Manuscript Author Manuscript Author Manuscript

Table 2

Material parameters for mitral leaflets and chordae tendineae.

Mitral Leaflets

	C_{01}	K_1	k_2	C_{10}	Kappa	Theta(^{O})	D	R^2
AML	61.303	9.295 9	9.684	0.285	0.333	0	5.0e-4	0.956
PML	33.191	10.756 4	8.495	0.101	0.089	2	5.0e-4	0.964

Chordae Tendineae

	U1(Mpa)	A1	U2(Mpa)	A2	U3(Mpa)	A3	R^2
AM	17.824	17.808	17.660	17.797	17.592	17.768	0.988
AS	24.342	11.338	10.332	11.167	14.914	11.188	0.972
PB	10.256	16.579	10.654	16.554	10.671	16.554	0.999
PM	12.995	15.651	13.083	15.683	12.870	15.662	0.976

AML – Anterior Mitral Leaflet; **PML** – Posterior Mitral Leaflet; AM – Anterior marginal; **AS** – Anterior strut; **AB** – Anterior basal; **PB** – Posterior basal; **PM** – Posterior Marginal.

Author Manuscript Author Manuscript Author Manuscript Author Manuscript

Table 3

Mitral valve measurements and comparison to 3D Echocardiography by Grewal *et al* [1] and by Gogoladze et al. [2].

	Raw MSCT images		FE model (NP)	FE model (P)	Literature			
Unit (mm)	**Diastole**	**Systole**	**Systole**	**Systole**	**NORMAL Diastole [1]**	**NORMAL Systole [1]**	**NORMAL systole [2]**	**FMR systole [2]**
Annular Perimeter	120.55	119.67	120.52		123.9 ± 8.9	127.6 ± 9.5	-	-
ID	36.04	39.10	38.25		39.2 ± 1.9	38.7 ± 2.6	-	-
AD	36.11	33.51	32.22		32.7 ± 3.3	32.7 ± 2.7	31.80 ± 4.80	32.40 ± 4.20
Intertrigonnal dist	26.56	28.05	27.45		-	-	-	-
AH	3.02	4.02	4.73		5.6 ± 2.2	7.9 ± 2.2	-	-
L_C	-	0	1.37	0	-	-	4.9 ± 3.8	1.5 ± 2.2
D_C	-	8.75	9.18	10.22	-	-	5.2 ± 1.3	9.7 ± 3.3
APM – PPM distance								
Lateral	38.73	36.61	-	-	-	-	-	-
Apical	0.14	0.42	-	-	-	-	-	-
APM to left trigone	31.65	30.98						
PPM to right trigone	27.74	25.79						

ID – Intercommissural Diameter, **AD** – Anteroposterior Diameter; **AH** – Annular Height; **L_C** – Coaptation Length; **D_C** – Coaptation Depth; **NP** – No pretension, **P** – Pretention.

Author Manuscript Author Manuscript Author Manuscript Author Manuscript

Table 4

Summary of average chordae tendineae systolic tension forces.

Chordae Force (N)	Current FE Model	In Vitro Experiments by Jimenez et al. [47]
AML marginal	0.30	0.35 ± 0.16
AML strut	0.67	0.95 ± 0.35
PML marginal	0.20	0.06 ± 0.05
PML basal	0.38	0.31 ± 0.25